

An automated tool for detection of FLAIR-hyperintense white-matter lesions in Multiple Sclerosis

Paul Schmidt ^{a,b,1}, Christian Gaser ^{c,d,1}, Milan Arsic ^a, Dorothea Buck ^a, Annette Förtschler ^e, Achim Berthele ^a, Muna Hoshi ^a, Rüdiger Ilg ^a, Volker J. Schmid ^b, Claus Zimmer ^e, Bernhard Hemmer ^a, Mark Mühlau ^{a,*}

^a Department of Neurology, Technische Universität München, Munich, Germany

^b Department of Statistics, Ludwig-Maximilian-University, Munich, Germany

^c Department of Psychiatry, Friedrich-Schiller-University, Jena, Germany

^d Department of Neurology, Friedrich-Schiller-University, Jena, Germany

^e Department of Neuroradiology, Technische Universität München, Munich, Germany

ARTICLE INFO

Article history:

Received 21 April 2011

Revised 28 October 2011

Accepted 9 November 2011

Available online xxx

Keywords:

Lesion segmentation

FLAIR

Multiple Sclerosis

Voxel-based morphometry

ABSTRACT

In Multiple Sclerosis (MS), detection of T2-hyperintense white matter (WM) lesions on magnetic resonance imaging (MRI) has become a crucial criterion for diagnosis and predicting prognosis in early disease. Automated lesion detection is not only desirable with regard to time and cost effectiveness but also constitutes a prerequisite to minimize user bias. Here, we developed and evaluated an algorithm for automated lesion detection requiring a three-dimensional (3D) gradient echo (GRE) T1-weighted and a FLAIR image at 3 Tesla (T). Our tool determines the three tissue classes of gray and white matter as well as cerebrospinal fluid from the T1-weighted image, and, then, the FLAIR intensity distribution of each tissue class in order to detect outliers, which are interpreted as lesion beliefs. Next, a conservative lesion belief is expanded toward a liberal lesion belief. To this end, neighboring voxels are analyzed and assigned to lesions under certain conditions. This is done iteratively until no further voxels are assigned to lesions. Herein, the likelihood of belonging to WM or GM is weighed against the likelihood of belonging to lesions. We evaluated our algorithm in 53 MS patients with different lesion volumes, in 10 patients with posterior fossa lesions, and 18 control subjects that were all scanned at the same 3T scanner (Achieva, Philips, Netherlands). We found good agreement with lesions determined by manual tracing (R2 values of over 0.93 independent of FLAIR slice thickness up to 6 mm). These results require validation with data from other protocols based on a conventional FLAIR sequence and a 3D GRE T1-weighted sequence. Yet, we believe that our tool allows fast and reliable segmentation of FLAIR-hyperintense lesions, which might simplify the quantification of lesions in basic research and even clinical trials.

© 2011 Published by Elsevier Inc.

Introduction

Multiple Sclerosis (MS) is an inflammatory demyelinating disease of the central nervous system that affects over 2.5 million people worldwide and is one of the leading causes of serious neurologic disability in young adults (Confavreux and Vukusic, 2008; Weiner, 2009). The disease is characterized by unpredictable episodes of clinical relapses and remissions followed by continuous progression of disability over time (secondary progressive MS) in most instances (Compston and Coles, 2008; Noseworthy et al., 2000). Demyelinating lesions (plaques) within cerebral white matter (WM) are the hallmark of MS and its detection by T2-weighted magnetic resonance imaging (MRI) has become a

crucial diagnostic criterion (Polman et al., 2011). Moreover, T2-hyperintense lesion volume has been demonstrated to correlate with severity of symptoms, progression of disability and gray-matter (GM) atrophy (Bendfeldt et al., 2010; Chard et al., 2002; Fisher et al., 2008; Fisniku et al., 2008). Accordingly, T2-hyperintense lesion volume has been of interest in basic research and has been determined in most pivotal trials on disease-modifying drugs since the late nineties (Ebers, 1998; Jacobs et al., 2000; Kappos, 1998).

Automatization of T2-hyperintense lesion volumetry is desirable with regard to time and cost effectiveness but also constitutes a prerequisite to minimize user bias. Up to now, a number of algorithms have been proposed (Table 1) but no gold standard has been established. Therefore, in the vast majority of clinical trials, lesions were traced manually slice by slice – sometimes with the help of semi-automated tools for contour detection.

Here, we aimed at the development and validation of an automated algorithm for segmentation of T2-hyperintense WM lesions in MS based on a T2-weighted fluid-attenuated (FLAIR) and a three-

* Corresponding author at: Department of Neurology, Klinikum rechts der Isar, Technische Universität München, Ismaningerstr. 22, D-81675 Munich, Germany. Fax: +49 89 4140 4867.

E-mail address: muehlau@lrz.tum.de (M. Mühlau).

¹ These authors contributed equally to this work.

Table 1
Studies on automated lesion segmentation in MS.

References in chronological order	Method	Sequences	Validation technique number of patients/controls
(Van Leemput et al., 2001)	EM alg. with MRF and OD	T1, T2, PD	Manual segmentation 23 /
(Ferrari et al., 2003)	SVM	T1, T2, FLAIR	Manual segmentation 18 /
(Anbeek et al., 2004)	KNN	T1, T2, PD, FLAIR	Manual segmentation 19 /
(Ait-Ali et al., 2005)	Robust EM, trimmed likelihood estimator and OD	T1, T2, PD	Simulated data (BrainWeb) / /
(Li et al., 2005)	EM alg. with MRF	T1, T2, FLAIR	Visual inspection 6 2
(Wu et al., 2006)	Supervised KNN classifier	T1, T2, PD	Manual segmentation 6 /
(Herskovits et al., 2008)	Classification statistics based on training data	T1, T2, FLAIR	Manual segmentation 1
(Khayati et al., 2008)	Adaptive mixture model	FLAIR	Manual segmentation 20 /
(Wels et al., 2008)	Probabilistic boosting tree	T1, T2, FLAIR	Manual segmentation 6 /
(Freifeld et al., 2009)	Constrained Gaussian mixture model and OD	T1, T2, PD or T1, T2, PD, FLAIR	Mainly simulated data (BrainWeb) manual segmentation ? /
(Garcia-Lorenzo et al., 2009)	Automatic multimodal graph cuts	T1, T2, PD	Simulated (BrainWeb) and manual segmentation 10 /
(Akselrod-Ballin et al., 2009)	Decision forest classifier based on training data	T1, T2, PD FLAIR	Manual segmentation 25 / 16
(Geremia et al., 2010)	Spatial decision forests	T1, T2, FLAIR	Manual segmentation 20 /

Note. In two online libraries (<http://apps.isiknowledge.com>, <http://www.ncbi.nlm.nih.gov/>), we searched for the combination of the following terms: Multiple Sclerosis, MRI, automated (or automatic), lesion. The retrieved articles including their references were then studied. alg., algorithm; EM, expectation maximization; KNN, K-nearest neighbor; MRF, Markov random field; OD, outlier detection; SVM, support vector machine.

dimensional (3D) gradient echo (GRE) T1-weighted sequence derived from a 3 Tesla (T) scanner. Such protocols have increasingly been used in clinical practice, since evidence suggests superiority of 3 T scanners over those with lower field strength (Wattjes and Barkhof, 2009; Wattjes et al., 2006a) and superiority of FLAIR sequences over conventional T2-weighted sequences (Bakshi et al., 2001; Filippi et al., 1996; Stevenson et al., 1997; Wattjes et al., 2006b; Woo et al., 2006).

Materials and methods

Subjects

The study was performed in accord with the Helsinki Declaration of 1975 and approved by the local ethics committee. Beforehand, written informed consent was obtained from the control subjects to participate and from the patients to subject their MRI scans, acquired in routine clinical practice, to scientific studies.

We obtained MRI scans from 18 control subjects (age in years: 23–58; median, 30; 32.6 ± 10.6), and 52 MS patients (age in years: 23–64; median, 41; 32.6 ± 11.4 ; EDSS: 0–4; median, 2). Five of the 52 MS patients were also included in another group of 10 MS patients with posterior fossa lesions according to their medical records (age in years: 24–64; median, 36; 37.9 ± 13.1 ; EDSS: 0–4; median, 2).

Magnetic resonance imaging

All brain images were acquired on the same 3 T scanner (Achieva, Philips, Netherlands). We used a 3D GRE T1-weighted sequence (orientation, 170 contiguous sagittal 1 mm slices; field of view, 240×240 mm; voxel size, $1.0 \times 1.0 \times 1.0$ mm; repetition time (TR), 9 ms; echo time (TE), 4 ms), and a 3D FLAIR sequence (orientation, 144 contiguous axial 1.5 mm slices; field of view, 230×185 mm; voxel size, $1.0 \times 1.0 \times 1.5$ mm; TR, 10^4 ms; TE, 140 ms; TI, 2750 ms). For additional analyses (see Evaluation section), FLAIR images were also resliced to 3 and 6 mm in axial and sagittal orientations.

Lesion segmentation algorithm

For better understanding, we give a conceptual overview of the three major steps of our algorithm in this paragraph (Fig. 1). First (for details see Preprocessing with already available software section), preprocessing is performed with the standard software of SPM8 and its extension VBM8. To surpass smoothing of the individual images by warping, the algorithm operates in the space of the original T1-

weighted image, i.e. in native space. Each voxel of the individual native T1-weighted image is assigned to one of the three tissue classes of GM, WM, or CSF. The FLAIR image is bias-corrected for MR field inhomogeneity and coregistered to the T1-weighted image. Since a-priori probability of each voxel of belonging to WM, the tissue class containing the lesions, is utilized later, the SPM tissue probability map of WM (TPM_{WM}) is warped into native space. Second (for details see Lesion belief maps and initialization section), FLAIR intensity distributions are calculated for each of the three tissue classes to detect FLAIR-hyperintense outliers which are further weighed according to their spatial probability of being WM. This results in lesion belief maps (B_{WM} , B_{CSF} , B_{GM}). Now, the three lesion belief maps are summed up (B). The binary version of the GM lesion belief map is used as a seed, the initial lesion map (L_{init}). Third (for details see Lesion growing section), the lesion growth model expands the L_{init} , a conservative assumption for lesions, toward the lesion belief map (B), a liberal assumption for lesions. To this end, neighboring voxels are analyzed and assigned to lesions under certain conditions. This is done iteratively until no further voxels are assigned to lesions. Herein, the likelihood of belonging to WM or GM is weighed against the likelihood of belonging to lesions. Two model parameters had to be set (for details see Determination of the initial threshold and of the final threshold section). The algorithm was programmed in MATLAB (www.mathworks.de/products/matlab/). We provide a pseudo-code description of our algorithm in Appendix A1 and performance parameters in Appendix A2. In the following subsections, we describe our algorithm in detail. Alternatively, the reader may continue with the Evaluation section.

Preprocessing with already available software

We use SPM8 (<http://www.fil.ion.ucl.ac.uk/spm/>) and its VBM8 toolbox (<http://dbm.neuro.uni-jena.de/vbm>). At option, VBM8 can provide images of the same modality which are bias-corrected for MR field inhomogeneity either in native space or normalized to MNI space; further, partial volume estimate (PVE) images (Tohka et al., 2004) can be generated which are either in native space or normalized to MNI space. In this protocol, images are corrected for bias-field inhomogeneity, registered using linear (12-parameter affine) and nonlinear transformations, and tissue-classified into GM, WM, and CSF within the same generative model (Ashburner and Friston, 2005). This segmentation procedure is further refined by accounting for partial volume effects (Tohka et al., 2004), by applying adaptive maximum a posteriori estimations (Rajapakse et al., 1997), and by applying hidden Markov random field (MRF) model (Rajapakse et al., 1997) as proposed recently (Lüders et al., 2009).

Lesion Segmentation Algorithm

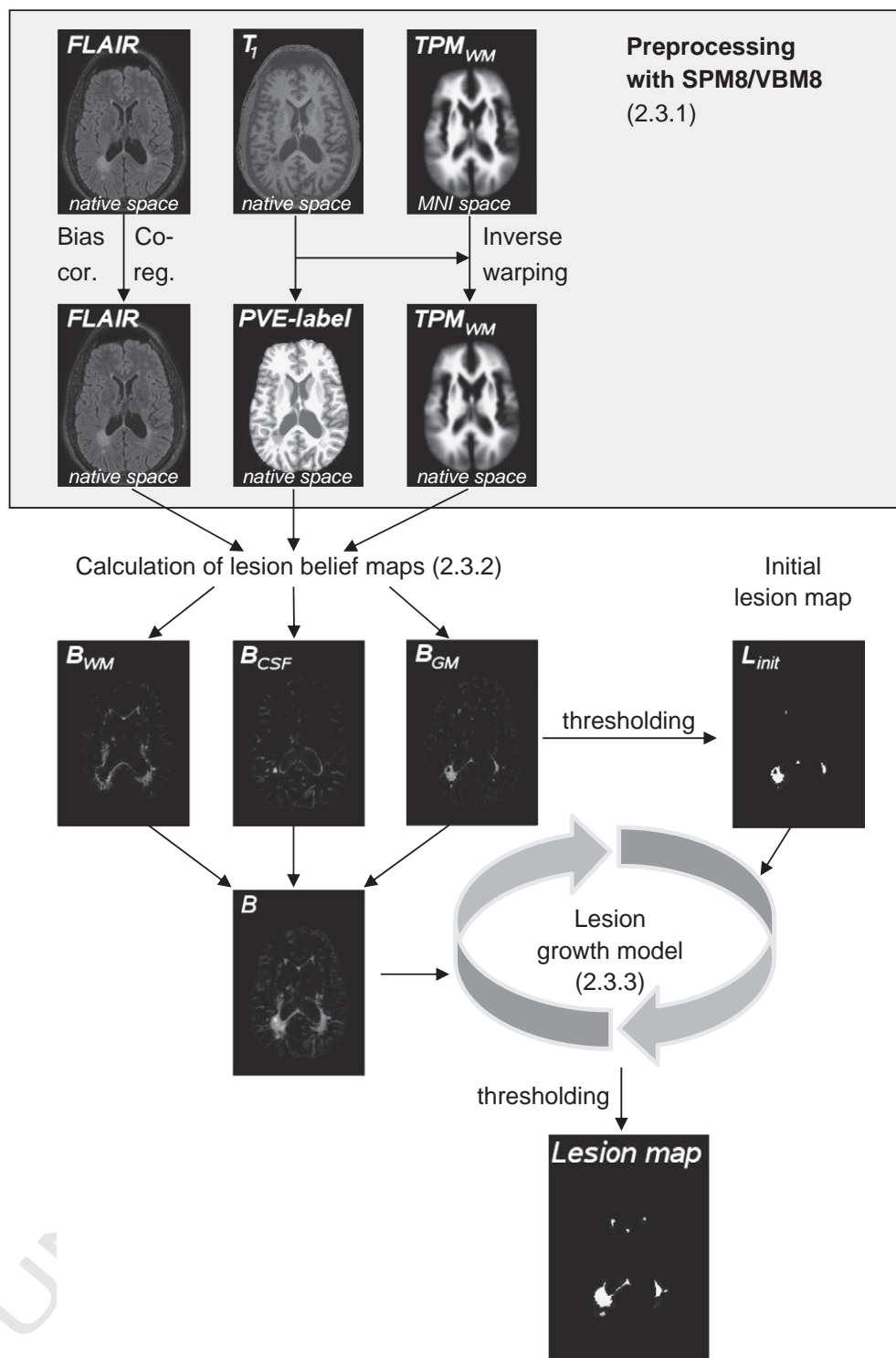


Fig. 1. The flow diagram of the lesion segmentation algorithm is shown. Preprocessing with the standard software of SPM8 and VBM8 is illustrated in the gray box. At first, the individual native T1 image is used to generate a partial volume estimate (PVE) label. To this end, some normalization is necessary. To surpass smoothing of the individual images by warping, the algorithm operates in native space exclusively. Thus, preprocessing includes the coregistration of FLAIR images to T1 images, PVE label estimation but output in native space, as well as inverse warping of the white matter (WM) tissue probability map (TPM_{WM}) to native space by the use of the inverse deformation matrix derived from PVE label estimation. Next, FLAIR intensity distribution is calculated for each of the three tissue classes to detect FLAIR-hyperintense outliers which are further weighed according to their spatial probability of being WM resulting in belief maps (B_{WM} , B_{CSF} , B_{GM}). Now, the three lesion belief maps are summed up (B). The binary version (threshold $\kappa=0.3$) of the GM lesion belief map is used as initial lesion map (L_{init}). Finally, the lesion growth model expands the L_{init} , a conservative assumption for lesions, toward the lesion belief map (B), a liberal assumption for lesions (see text for details).

157 For tissue classification, the T1-weighted image is used to estimate
 158 a PVE image in which a number in the range between 1 and 3 is
 159 assigned to each voxel. In accordance with image intensity, the
 integers (1, 2, 3) stand for CSF, GM and WM, respectively. Values be- 160
 tween those integers indicate the partial volume effect. Of note, voxel 161
 values are estimated primarily on the basis of intensity values. Yet a- 162

priori (i.e. spatial) information on tissue-classes is used for scalp editing so that some normalization is necessary although our algorithm only uses the PVE image in native space. For normalization, we choose the option of low-dimensional warping since visual inspection of the PVE images, normalized this way, did not yield a single case in which MS lesions disturbed normalization. Next, the FLAIR image is bias-corrected by the same routine of VBM8 and coregistered to the native T1-weighted image by the standard routine of SPM8. Since a-priori probability of each voxel belonging to WM, the tissue class containing the lesions, is utilized later, the SPM tissue probability map of WM (TPM_{WM}) is warped into native space by the use of the inverse deformation matrix derived from PVE label estimation. We will refer to this image as native TPM_{WM} .

176 *Lesion belief maps and initialization*

177 By the use of the PVE image, we estimate the distributions of FLAIR
178 intensity for each tissue class. Of note, we expect lesion voxels to be-
179 have as hyperintense outliers from these distributions. Let x_i denote
180 the estimated PVE label of voxel i , we then assign a discrete label z_i
181 to each voxel as follows:

$$z_i = \begin{cases} \text{CSF,} & \text{if } x_i < 1.5 \\ \text{GM,} & \text{if } 1.5 \leq x_i < 2.5 \\ \text{WM} & \text{if } x_i \geq 2.5. \end{cases} \quad (1)$$

183 Next, FLAIR images are scaled via voxel-wise division by the mean
184 FLAIR intensity of the GM class ($z_i = \text{GM}$). Let $y = (y_1, \dots, y_n)$ denote
185 the scaled FLAIR intensities. Further, we denote the means of y
186 along the three tissue classes by $\bar{y}_k, k \in \{\text{CSF, GM, WM}\}$. The lesion be-
187 lief value for voxel i represents the amount of hyperintensity in terms
188 of the distance from the class mean \bar{y}_k weighted by the estimated PVE
189 label and by the a-priori (i.e. spatial) probability for WM:

$$b_{k,i} = (y_i - \bar{y}_k)^+ \cdot x_i \cdot Pr(z_i = \text{WM})$$

192 Here $(y_i - \bar{y}_k)^+$ is $y_i - \bar{y}_k$ if $y_i > \bar{y}_k$ and zero otherwise and $Pr(z_i =$
193 $\text{WM})$ is the probability that voxel i belongs to WM according to
194 the native TPM_{WM} . In this way, we obtain lesion belief maps $B_k =$
195 $\{b_{k1}, \dots, b_{kn}\}$ for all tissue classes k . Voxel values of B_{GM} increase
196 with (1) a high a-priori (i.e. spatial) probability for WM, (2) medium in-
197 tensity at T1, and (3) hyperintensity at FLAIR. Hence, increasing B_{GM}
198 values support the assumption that the respective voxel belongs to a
199 WM lesion. Similar interpretations can be made for B_{CSF} . Voxel values
200 of B_{CSF} increase with a high a-priori probability for WM, hypointensity
201 at T1, and hyperintensity at FLAIR. Hence, increasing B_{CSF} values support
202 the assumption that the respective voxel belongs to a WM lesion
203 (“black holes”). Likewise, voxel values of B_{WM} increase with a high a-
204 priori probability for WM, hyperintensity at T1, and hyperintensity at
205 FLAIR. Hence, increasing B_{WM} values support the assumption that the re-
206 spective voxel belongs to a WM lesion (“dirty WM”). Besides the lesion
207 belief maps for the three tissue classes, we compute a total lesion belief
208 map $B = \{b_1, \dots, b_n\}$ by summing up the three maps: $b_i = b_{CSF,i} + b_{GM,i} +$
209 $b_{WM,i}$. The lesion belief map B can be interpreted as a liberal assumption
210 of lesion voxels.

211 The proposed lesion growth algorithm requires initialization, i.e.
212 seed regions from where the lesions are expanded. Since extensive
213 preliminary experiments and analyses did not yield lesions without
214 any part assigned to GM according to the PVE label, we choose B_{GM}
215 for initialization of lesions after application of the threshold κ so
216 that we obtain the initial lesion map $L_{init} = \{l_{init,1}, \dots, l_{init,n}\}$ by

$$l_{init,i} = 1 \Leftrightarrow b_{GM,i} > \kappa.$$

218 This map can be interpreted as a conservative assumption of le-
220 sion voxels. Since the choice of the threshold κ is potentially critical,
221

we investigate the impact κ on the final segmentation in the
222 *Evaluation* section. 223

224 *Lesion growing*

225 Now, the lesion growth model expands the L_{init} , a conservative as-
226 sumption for lesions, toward the lesion belief map (B), a liberal as-
227 sumption for lesions. Each voxel in the neighborhood of the
228 initialized lesions is labeled *lesion* (Les) or *other*. This latter class con-
229 sists of the three main tissue classes CSF, GM and WM. Thus, the dis-
230 crete label z_i for voxel i can be either Les or $other$. We approximate the
231 distribution of Les by a gamma distribution with shape and scale pa-
232 rameters α and β , respectively, and the distribution of $other$ by a mix-
233 ture of three Gaussians:

$$p_{other}(y_i|\theta) = \sum_k \pi_k \cdot \phi(y_i|\mu_k, \sigma_k^2).$$

234 In this notation, ϕ stands for the probability density function of the
235 Gaussian (normal) distribution with mean μ_k and variance σ_k^2 and π_k
236 is the proportion of the k th class. The vector θ collects the parameters
237 μ_k and σ_k^2 for all tissue classes. Since the classification of voxel i in re-
238 spect to the three tissue classes CSF, GM, and WM is known from
239 Eq. (1), the unknown parameters in θ can be estimated using the
240 maximum likelihood estimators: 241 242

$$\hat{\mu}_k = \frac{1}{n_k} \sum_{i:z_i=k} y_i \quad \hat{\sigma}_k^2 = \frac{1}{n_k-1} \sum_{i:z_i=k} (y_i - \hat{\mu}_k)^2.$$

243 The mixture proportions are estimated by $\hat{\pi}_k = n_k/n$ where n is the
244 total amount of brain voxels that belong to either CSF or GM or WM. 245
246 The parameters of the gamma distribution are also estimated by max-
247 imum likelihood as it is implemented in the MATLAB function `gamfit`. 248
249 Next, we describe the way in which the initialized lesions are allowed
250 to grow toward the final lesion map. 251

252 We use an iterated growth algorithm. In each iteration, voxels that
253 share a common border with a lesion voxel are considered to be a le-
254 sion. Instead of accepting or rejecting the proposed value ($z_i = Les$)
255 the algorithm assigns the following value to the i th voxel: 256

$$\pi_i^{Les} = Pr(z_i = Les) = \min\left(1, \frac{p_{Les}(y_i|\hat{\alpha}^{(t-1)}, \hat{\beta}^{(t-1)}) \cdot b_i}{p_{other}(y_i|\hat{\theta}^{(t-1)})}\right) \quad (2)$$

257 Here, i stands for indices of voxels with at least one neighbor j
258 with $\pi_j^{Les} > 0$. The value b_i in Eq. (2) ensures that a lesion could only
259 grow along those voxels which have a positive lesion belief value. 260
261 With other words, lesions are only allowed to grow within our liberal
262 lesion assumption. After each iteration, the parameters in θ and α and
263 β are re-estimated. For the estimation of α and β only those voxels
264 with $\pi_i^{Les} \geq 0.5$ are considered. Likewise, the updating of $\hat{\theta}$ is based
265 on voxels with $\pi_i^{Les} < 0.5$. For initialized lesion voxels, we set $\pi_i^{Les} = 1$.
266 The algorithm stops when no more voxels with $\pi_i^{Les} > 0.01$ are ob-
267 served. This results in a lesion probability map. Next, we expand our
268 algorithm by incorporation of the information of neighboring voxels. 269

270 Assuming that a voxel, which is completely surrounded by lesion
271 voxels, is more likely to be part of a lesion than of the other classes,
272 we utilize a MRF. We will briefly summarize the important aspects
273 of MRFs that have been extensively reviewed elsewhere (Winkler, 271 Q2
272 2003). In a random field, the labels $z = (z_1, \dots, z_n)$ are viewed as a re-
273 alization of a collection of random variables $Z = (Z_1, \dots, Z_n)$ in which
274 each random variable has the domain L , or $L = \{Les, other\}$ in this
275 case. Z is a MRF if the following two conditions are met

- 276 1. $p(z) > 0$ for all possible realizations z ,
- 277 2. $p(z_i|z_{-i}) = p(z_i|z_N)$

While the first assumption is required for technical reasons, the second states that the probability of z_i , given all other labels, depends only on voxels that are in the neighborhood N_i of z_i . Here, z_{N_i} is the set of voxels that are in the neighborhood N_i , $z_{N_i} = \{z_i | i' \in N_i\}$. According to the Hammersley–Clifford–Theorem (Hammersley and Clifford, 1971), a MRF is equivalent to a Gibbs Random Field. Thus, its distribution follows a Gibbs distribution and the conditional distribution of z_i for a given neighborhood can be written as

$$p(z_i | z_{N_i}) = \frac{\exp\{-U(z_i | z_{N_i})\}}{\sum_{k \in L} \exp\{-U(k | z_{N_i})\}}. \quad (3)$$

Here, $U(k | z_{N_i})$ is the so-called energy function that is primarily responsible for the resulting segmentation. One simple choice for this energy function leads to the Ising model that has been extensively studied in the context of brain image segmentation by others (Zhang et al., 2001; Woolrich et al., 2005):

$$U(k | z_{N_i}) = \varphi \sum_{j \in N_i} I(z_j \neq z_i) \quad (4)$$

in which $I(a)$ is the indicator function that is 1 if statement a is true and 0 otherwise. This energy function favors the segmentation of voxel i as a lesion if more voxels in N_i are already marked as a lesion. Instead of discrete labels the proposed algorithm produces values $\pi_i^{Les}, \dots, \pi_n^{Les}$ in the interval $[0,1]$. Thus, integration of energy function (4) in our algorithm would require another threshold to produce a binary lesion map. To address this problem, we modify energy function (4) by using the probabilities of the neighboring voxels instead of the discrete labels:

$$U(\pi_i^{Les} | \pi_{N_i}^{Les}) = \varphi \sum_{j \in N_i} (1 - \pi_j^{Les}). \quad (5)$$

We follow the choice of others (Khayati et al., 2008; Li et al., 2005; Zhang et al., 2001) and choose $\varphi = 1$. To include the MRF in the lesion growth model, we use Eq. (3) as additional information and expand Eq. (2) to

$$\pi_i^{Les} = \min\left(1, \frac{p_{Les}(y_i | \hat{\alpha}^{(t-1)}, \hat{\beta}^{(t-1)}) \cdot b_i \cdot \exp(-\sum_{j \in N_i} (1 - \pi_j^{Les}))}{p_{Other}(y_i | \hat{\theta}^{(t-1)}) \cdot \exp(-\sum_{j \in N_i} \pi_j^{Les})}\right).$$

Determination of the initial threshold and of the final threshold

The initial threshold κ is a cutoff that produces the initial lesion map, L_{init} , from the GM lesion belief map, B_{GM} (see Preprocessing with already available software section). In detail, values near 0 imply many voxels (all voxels of GM with a TPM_{WM} value over 0 and with a FLAIR intensity value above GM average) whereas values around 1 imply a very conservative initialization. We tested the images of all patients with values of κ ranging from 0.05 to 0.95 with an increment of 0.05 (Fig. 2A). Applying values below 0.1 led to identification cortical hyperintensities which are inherent to FLAIR images whereas lesions were missed at values above 0.8. In conclusion, the effect of different κ values seemed to be limited in the range from 0.1 to 0.8. Yet, we analyzed the influence of κ on the agreement with manual segmentation (see Evaluation section) as measured with the Dice coefficient (DC). As shown in Fig. 2A, there is a plateau of DC values for κ values between 0.25 and 0.4. Eventually, we choose the value of 0.3 for κ , as it goes along with the greatest mean, the greatest minimum and the smallest bandwidth of DCs.

To enable comparison with manual segmentation (see Evaluation section), the lesion probability maps must be transformed into binary maps. To this end, we chose the threshold of 1.00. The distribution of

all voxels with lesion probability greater than 0 across all subjects (Fig. 2B) strongly suggested this threshold since there was a sharp increase in frequency of voxel values in the range from >0.95 to ≤ 1.00 compared to voxel values in the range from >0.90 to ≤ 0.95 ; further, of the latter class, 99.65% of the voxel values were 1.00.

Evaluation

Since no gold standard for segmentation of T2-hyperintense lesions exists, we compared our algorithm with a semi-automatic manual tracing pipeline, which is based on commercially available software (Amira 5.3.3, Visage Imaging, Inc.) and which has been applied for basic research studies (Bendfeldt et al., 2010) and clinical trials (Li et al., 2006). At first, the manual segmentation was independently performed by two investigators, who were blinded to the study group. Then, a difference image of the two binary lesion maps was generated for each subject and both experts together decided which differences were assigned to lesions or not.

We performed a correlation and regression analysis to compare the volumetric agreement between automated and manual segmentation. For better estimation of intercept, slope, and R2, we included the data of our control subjects. Since 3D acquisition of FLAIR sequences has not been used commonly, we repeated estimation of R2 after reslicing of the FLAIR images to 3 and 6 mm slice thickness in sagittal and axial orientations, respectively.

To determine agreement between automatic and manual segmentation, we used standard validation techniques (Anbeek et al., 2004; Ashburner and Friston, 2005). We extracted the true positives (TP) and true negatives (TN) as well as the false positives (FP) and false negatives (FN). Then, we calculated the similarity measures of sensitivity (SE), $SE = TP / (TP + FN)$, specificity (SP), $SP = TN / (TN + FP)$, and accuracy (AC), $AC = (TN + TP) / (TN + TP + FP + FN)$. Furthermore, we calculated the Dice coefficient (DC), which equally weighs the number of false negatives and false positives without accounting for true negatives (Dice, 1945; Zijdenbos et al., 1994):

$$DC = \frac{2 \cdot TP}{2 \cdot TP + FP + FN}.$$

All of these similarity measures have values between 0 and 1 with higher values indicating better quality.

Moreover, we analyzed a group of 10 MS patients with posterior fossa lesions and 18 control subjects.

Results

Based on T1-weighted and FLAIR images, T2-hyperintense WM lesions were segmented. Correlation analysis of lesion volumes (52 MS patients and 18 control subjects) derived from automated segmentation with those derived from manual tracing yielded excellent results with R2 values greater than 0.93 irrespective of orientation and slice thickness of the FLAIR sequence (Fig. 3, 3 mm slice thickness not shown). The slope of the regression line of 0.948 did not differ significantly from 1.0 (95% confidence interval, 0.892 to 1.004) and the intercept of -0.154 not from 0 (95% confidence interval, -1.04 to 0.732). Moreover, a high degree of agreement between manual tracing and automated segmentation was demonstrated with regard to sensitivity, specificity, accuracy, and DC (Table 2). To further evaluate differences between both methods with respect to size and location of the lesions, we determined the DC in the 52 MS patients and related them to the lesion volume indicating decreasing DCs with decreasing lesion volume (Fig. 4). However, in the patient group, 71% ($n = 37$) showed an excellent DC of greater than 0.7 (see Fig. 5 for 2 examples). Of the remaining 29% ($n = 15$), 10% ($n = 5$) had a DC below 0.6. Of the latter, the

Parameters of the lesion growth algorithm

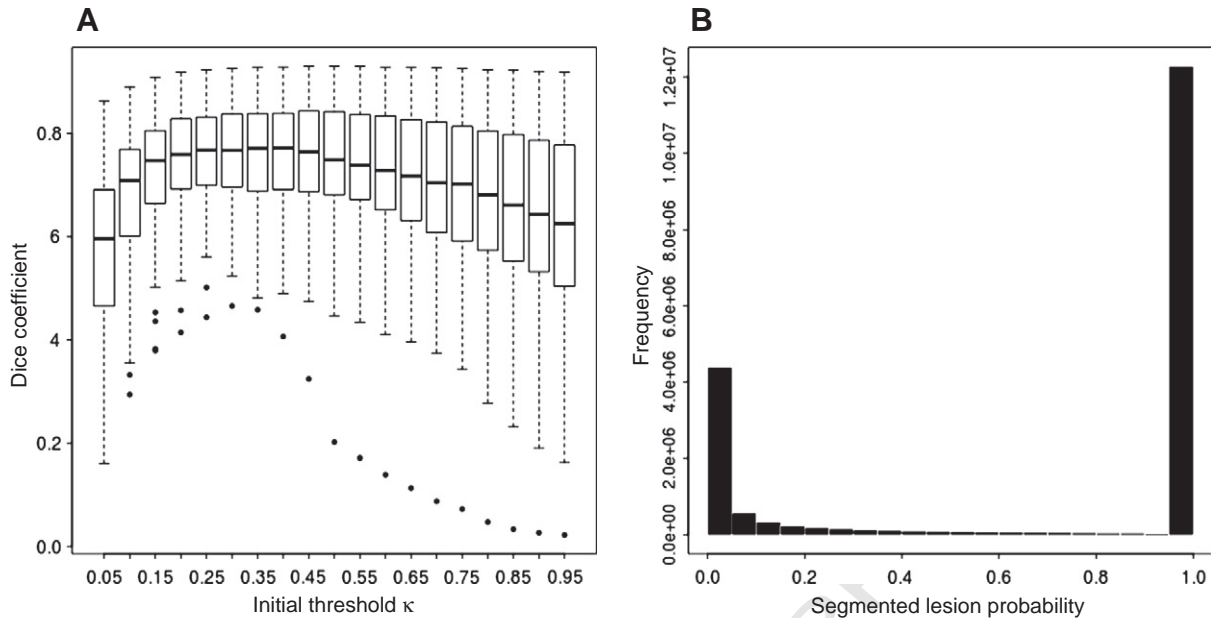


Fig. 2. Parameters of the lesion growth algorithm are shown. In Panel A, scatter plots of Dice coefficients from all patients over different initial thresholds κ are shown. The κ value of 0.3 goes along with Dice coefficients that show the greatest mean, greatest minimum, and smallest bandwidth. Panel B shows a histogram of the lesion probabilities of all voxels greater zero across all subjects. Note that 99.65% of the voxels in the range from >0.95 to ≤ 1.00 as represented by the right bar were 1.00 so that we chose the threshold of ≤ 1.00 .

393 lowest DC observed was 0.46 (Fig. 6, Panel A) and the highest lesion
 394 volume 13.44 ml (Fig. 6, Panel B). Analysis of posterior fossa lesions
 395 from 10 MS patients yielded that our algorithm detected 11 of 13
 396 posterior fossa lesions and 85% of the lesion volume (overall sensi-
 397 tivity, 0.85; overall DC, 0.94) but no false positive lesions. In the con-
 398 trol group, hyperintense foci volume ranged from 0.0 to 1.53 ml
 399 (0.25-Quantil, 0.029 ml; median, 0.058 ml; 0.75-quantil, 0.176 ml)
 400 and was almost exclusively limited to anterior and posterior peri-
 401 ventricular capping, as well as septal hyperintensity as illustrated
 402 by the images of the control subject with the highest hyperintense
 403 foci volume (Fig. 6, Panel C).

Discussion

404

We developed and evaluated an algorithm for automated segmen- 405
 tation of T2-hyperintense lesions in MS. We will review the strategy 406
 of our algorithm, assess the results of its evaluation, and, finally, spec- 407
 ulate on its potential opportunities. 408

Our algorithm (Fig. 1) requires high-resolution T1-weighted im- 409
 ages, which have been regarded most suitable for VBM (Ashburner 410
 and Friston, 2000) and which have become broadly available not 411
 only in neuroimaging research but also in clinical practice. It also re- 412
 quires FLAIR images, which have increasingly been used in MRI 413

Correlation Between Automated and Manual Lesion Segmentation At Different Slice Thickness

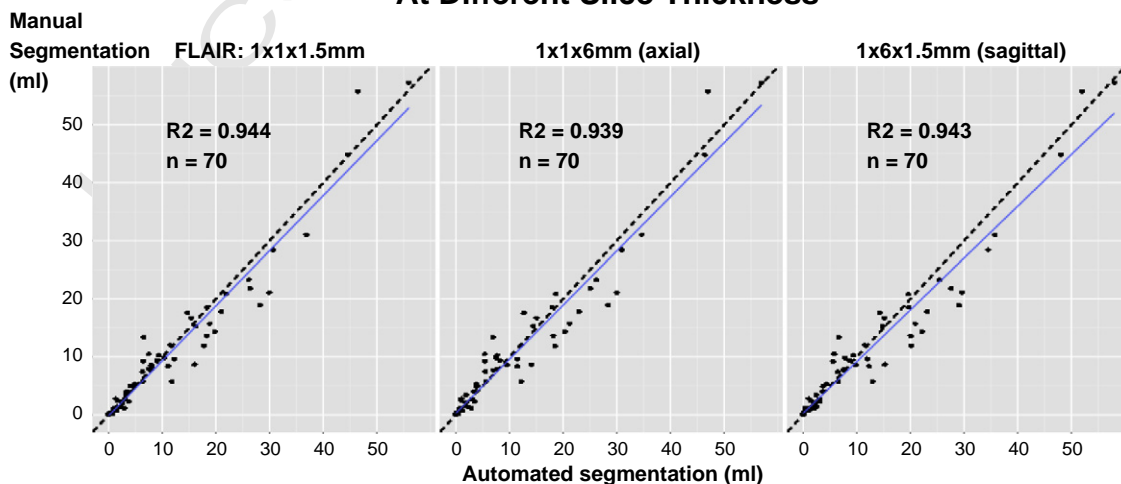


Fig. 3. Manually traced lesion volumes are plotted over automatically segmented lesion volumes at different orientations and slice thickness of the FLAIR sequence. Data from 52 MS patients and 18 control subjects are included. The respective R2 values are given.

t2.1 **Table 2**
 Statistics of similarity between automated segmentation and manual tracing derived from 53 MS patients.

t2.2 t2.3	Lesion volume	Sensitivity TP/(TP + FN)	Specificity TN/(TN + FP)	Accuracy (TN + TP)/(TN + TP + FN + FP)	Dice coefficient 2TP/(2TP + FP + FN)
t2.4	(ml)	(min. mean max.)	(min. mean max.)	(min. mean max.)	(min. mean max.)
t2.5	<5	0.4289 0.7332 0.9673	0.9997 0.9999 1.0000	0.9995 0.9998 1.0000	0.4658 0.6665 0.8025
t2.6	5–10	0.3889 0.7592 0.9497	0.9994 0.9998 1.0000	0.9990 0.9995 0.9999	0.5243 0.7594 0.8910
t2.7	10–15	0.7359 0.8870 0.9655	0.9991 0.9996 0.9999	0.9986 0.9993 0.9997	0.6738 0.8157 0.8727
t2.8	>15	0.9012 0.9494 0.9841	0.9990 0.9994 0.9997	0.9990 0.9993 0.9997	0.7838 0.8498 0.9253
t2.9	Total	0.3889 0.8033 0.9841	0.9990 0.9997 1.0000	0.9986 0.9995 1.0000	0.4658 0.7531 0.9253

t2.10 Note. FN, false negative; FP, false positive; min., minimum; max., maximum; TN, true negative; TP, true positive.

414 protocols for MS patients (Filippi et al., 1996; Stevenson et al., 1997;
 415 Wattjes et al., 2006b). Further, T1-weighted images were based on a
 416 GRE sequence as commonly applied at 3 T. In preliminary experi-
 417 ments, we failed to establish a robust segmentation of MS lesions
 418 from a single sequence since the algorithms applied attributed a con-
 419 siderable number of voxels to the lesion compartment in any case
 420 which resulted in tremendous false positive misclassification of vox-
 421 els to the lesion class especially in patients with low lesion volume
 422 and also in control subjects. Inspired by van Leemput et al. (Van
 423 Leemput et al., 2001), we surpassed lesion misclassification by incor-
 424 porating two sequences in our algorithm. At first, we assigned all vox-
 425 els to one of the three tissue classes of GM, WM, and CSF by the use of
 426 PVE labels derived from T1-weighted images, then, estimated the distri-
 427 bution of FLAIR intensities for each tissue class separately, and, finally,
 428 detected FLAIR hyperintense outliers within each tissue class.
 429 This way, the number of voxels correctly assigned to lesions can
 430 vary from zero to large values. To account for variable intensity with-
 431 in FLAIR images with regard to both normal tissue and lesions, we
 432 created an iterative algorithm that expanded the lesion belief from a
 433 conservative assumption toward a liberal assumption by voxel-wise
 434 weighing the likelihood of belonging to gray or white matter against
 435 the likelihood of belonging to lesions. Further, a hidden MRF segmen-
 436 tation model as well as a priori knowledge on WM location was

437 incorporated. It may seem surprising that our algorithm starts with
 438 the binary lesion belief map derived from the GM tissue class since
 439 this implies the assumption of, at least, some T1-hypointense voxels
 440 within every lesion. In contrast, evidence suggests that not all T2-
 441 hyperintense MS lesions are T1-hypointense (Bagnato et al., 2003;
 442 Sahraian et al., 2009). However, respective studies on these T1-
 443 hypointense lesions, also called black (or dark) holes, have almost ex-
 444 clusively been performed at field strengths of up to 1.5 T with turbo
 445 spin echo sequences whereas we applied a GRE sequence at 3 T and
 446 did not observe lesions without a T1-hypointense part. Of note, the
 447 initial lesion estimate is allowed to expand toward voxels, which
 448 are not T1-hypointense so that a lesion must only display a T1-
 449 hypointense part rather than complete T1-hypointensity. Based on
 450 our experience of possibly tremendous misclassification particularly
 451 in patients with low lesion volume, we also evaluated our algorithm
 452 with real data including control subjects, and patients with lesion vol-
 453 umes ranging from low to high.

454 Intriguingly, evaluation of an algorithm on MS lesion segmen-
 455 tation is hampered by the lack of a commonly accepted gold standard
 456 so that we compared the results derived from our algorithm with
 457 those derived from manual tracing by the use of a contour detection
 458 tool as suggested by others (Bendfeldt et al., 2010; Li et al., 2006).
 459 Mere correlation analyses of both methods showed excellent results
 460 (Fig. 3). The high R2 value indicates that both results share more
 461 than 93% of their variability. Furthermore, neither the slope differed
 462 significantly from 1 nor the intercept from zero suggesting that the le-
 463 sion extent determined by our algorithm largely resembles what an
 464 experienced examiner assigns to be a lesion. Yet mere correlation
 465 measures of global lesion volumes are insufficient for evaluation
 466 since they measure association of overall volume but not spatial
 467 agreement (Bartko, 1991). Therefore, we calculated the standard val-
 468 idation parameters of sensitivity, specificity, accuracy, and Dice coef-
 469 ficient (Table 2). Of note, the validation parameters as determined
 470 here are based on volumes, i.e. 3D data, so that they may seem to un-
 471 derstate the quality of our algorithm. For example, since lesion bor-
 472 ders are often fuzzy, it is well conceivable that the radius of a small
 473 lesion is measured to be 3 mm by the algorithm under investigation
 474 and 4 mm by the algorithm taken as the gold standard resulting in a
 475 sensitivity of 0.42 ($3^3/4^3$). This value nearly equals the lowest sensi-
 476 tivity measured in our patients (0.43); hence, sensitivity of our algo-
 477 rithm can be regarded to be very good. On the other hand, the
 478 measures of specificity and accuracy are excellent with regard to
 479 the mere numbers but still of little value since these parameters are
 480 strongly influenced by the number of true negatives, which is inher-
 481 ently very large as is the volume of the whole brain compared to
 482 the lesion volume. Only the DC equally weighs the number of false
 483 positives and false negatives without accounting for the absolute
 484 number of true negatives so that this similarity measure seems
 485 most suitable to evaluate the overall quality of our lesion segmen-
 486 tation algorithm. Nevertheless, the DC has two limitations. 1) In our
 487 study, DC determination becomes more critical with decreasing le-
 488 sion volume which was also reported by others (Anbeek et al.,
 489 2004; Wu et al., 2006). This is well conceivable assuming that lesion

Dice Coefficients Over Lesion Volumes (52 MS Patients)

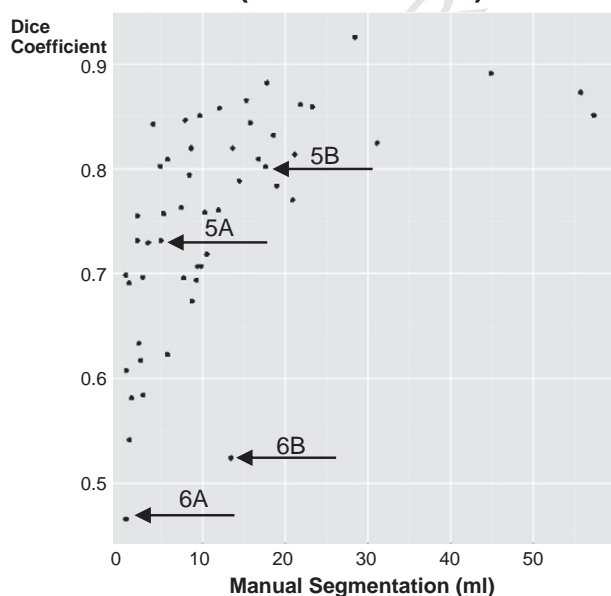


Fig. 4. Dice coefficients (DCs) of 52 patients are plotted over lesion volumes derived from manual tracing. The points indicated by numbered arrows correspond to Panels of Figs. 5 and 6.

Lesion Segmentation –Examples of 2 MS Patients

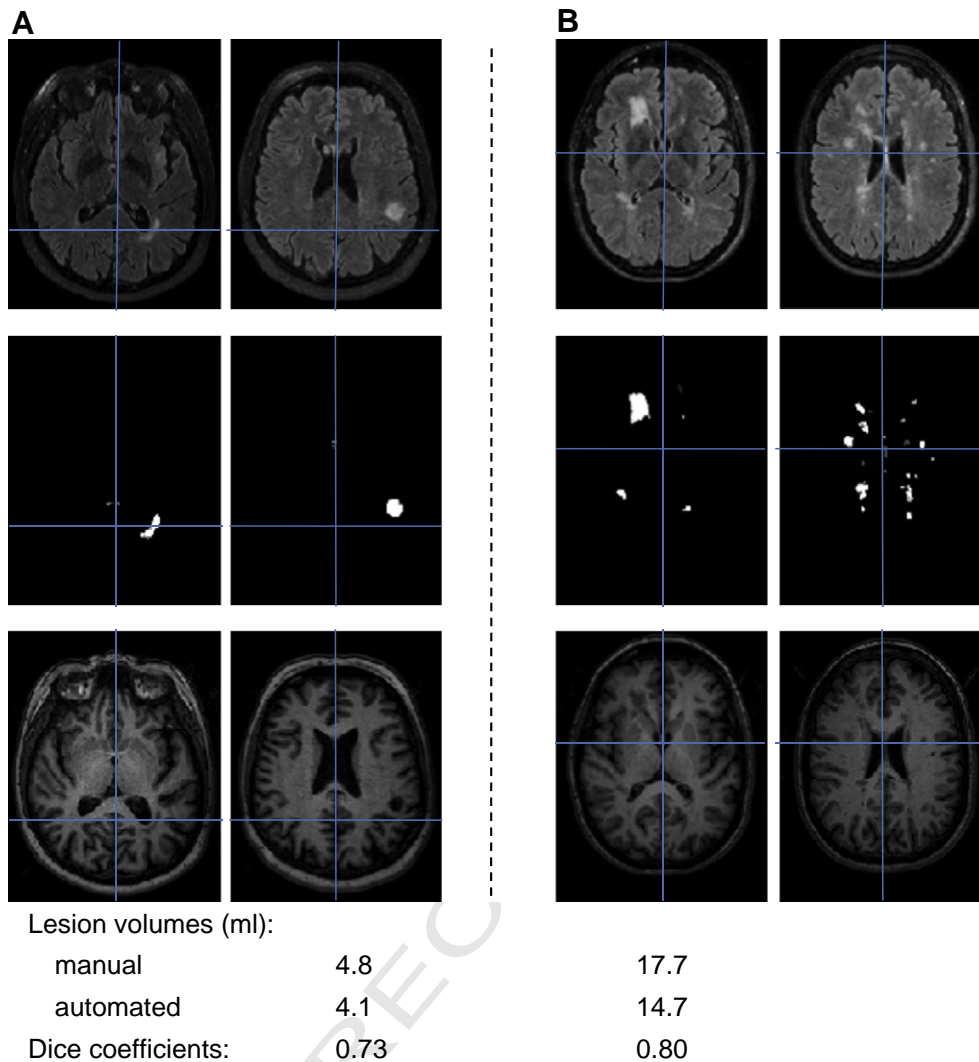


Fig. 5. Exemplary lesion segmentation is displayed from two MS patients with Dice coefficients over 0.7 (Panels A and B). Two axial slices are shown for each patient (upper row, FLAIR images; middle row, lesion maps; lower row, T1-weighted images). Panel letters correspond to arrows in Fig. 4. Lesion volumes and Dice coefficients are given at the bottom.

borders are determined with equal absolute errors irrespective of lesion size. This is likely to apply for our algorithm and, possibly even more so, for manual tracing (Woo et al., 2006) as also illustrated by our outlier patients (arrows in Fig. 4, Panels A and B of Fig. 6) in whom low DC values result from both false positives and false negatives. Further, in the extreme case, in which no lesion exists and no lesion is detected, as was the case in 1 of our 18 control subjects, the DC is not even defined (division by zero), although the result is perfect. 2) Apart from the fact that higher DC values imply better agreement, no commonly accepted rules on the interpretation of the DC exist. Some authors regard DC values over 0.7 as “excellent” (Anbeek et al., 2004; Bartko, 1991) others regard DC values over 0.4 as “moderate”, over 0.6 as “substantial”, and over 0.8 as “almost perfect” (Landis and Koch, 1977) while others emphasize that “conventional interpretative guidelines” may be misleading as DC values “obtained from samples with different base rates may not be comparable” (Uebersax, 1987). In addition, we evaluated our algorithm separately with regard to lesions in the posterior fossa because two studies found FLAIR imaging to be less sensitive here (Filippi et al., 1996; Stevenson et al., 1997). Although this finding lacked significance in a later study at 3 T (Wattjes et al., 2006b), we speculated that difficulties in detecting posterior fossa lesions could come more into play

when applying an automated tool which was the case to some degree as 2 of 13 lesions were missed. Yet our patients with posterior fossa lesions were selected according to their medical records which were also based on conventional T2-weighted images. Our examiners may have detected posterior fossa lesions more easily at FLAIR images knowing that lesions are likely to exist. Hence, sensitivity values for posterior fossa lesions possibly reflect lower sensitivity of FLAIR compared to conventional T2-weighted sequences to some degree. Moreover, we applied our algorithm in 18 control subjects. Here, the hyperintensities identified were almost exclusively limited to anterior and posterior periventricular capping, as well as septal hyperintensity. These results are well in accordance with a study on normal findings on FLAIR images at 3 T (Neema et al., 2009). In conclusion, our degree of agreement with manual tracing is remarkably good given that most DC values exceeded 0.7, that the DC values below 0.6 were observed almost exclusively in patients with low lesion volume, that most posterior fossa lesions were detected, and that no misclassification occurred in control subjects.

Finally, we repeated our evaluation analyses with the same images after reslicing of the FLAIR images to larger slice thickness at different orientations, since 3D FLAIR sequences have not been broadly established. This yielded highly comparable R2 values. These results

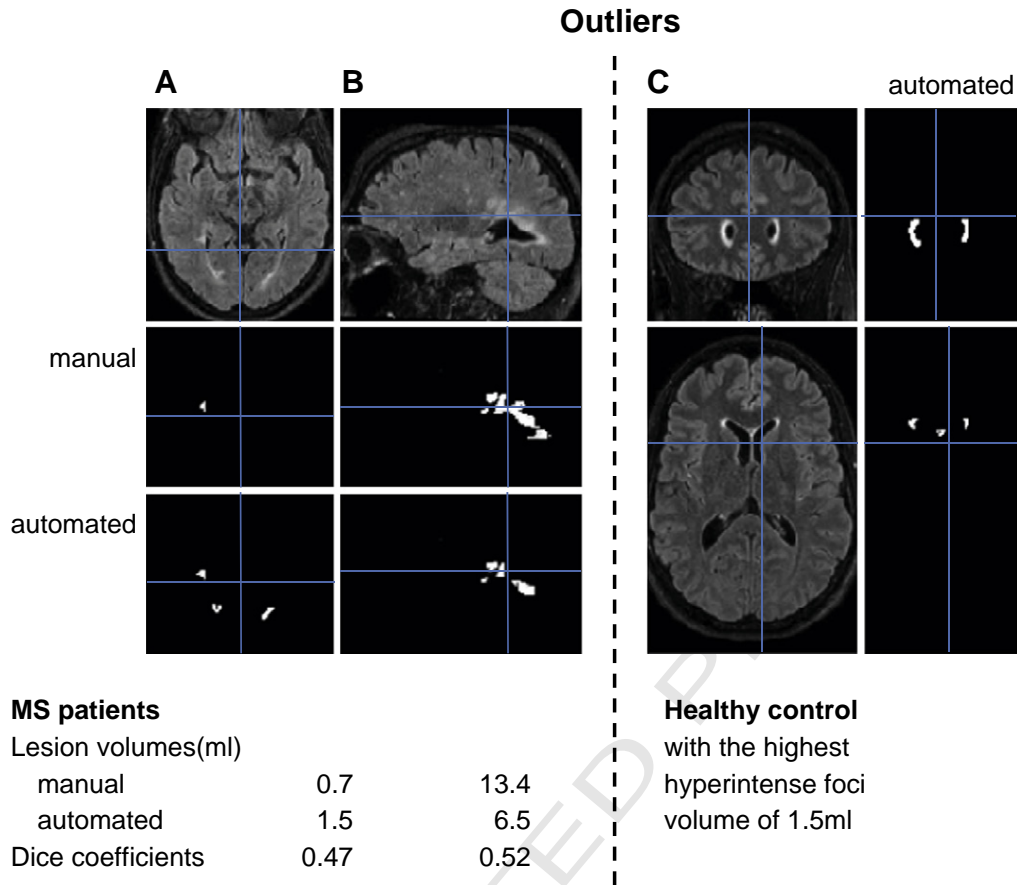


Fig. 6. Outliers of lesion segmentation are shown. Panel letters correspond to arrows in Fig. 4. Panel A shows the patient with the lowest Dice coefficient (DC), which results from posterior periventricular lesions detected by automated segmentation but not by manual tracing. Panel B shows the patient with the highest lesion volume among those with a DC below 0.6; the lesion volume results from many lesions, of which the manually segmented lesions appear to be larger. Panel C shows the control subject with the highest hyperintense foci volume which is restricted to anterior periventricular capping and septal hyperintensity. Lesion volumes and Dice coefficients are given at the bottom.

534 suggest that our algorithm may also operate well on data derived
 535 from protocols of other 3 T scanners based on a 3D GRE T1-
 536 weighted and a conventional FLAIR sequence. In this way, our tool
 537 may help to eventually take advantage of modern MRI protocols for
 538 MS patients in basic research and even clinical trials. However,
 539 these potential opportunities require validation with data from
 540 other protocols based on a conventional FLAIR sequence and a 3D
 541 GRE T1-weighted sequence at 3 T. Currently, we are programming
 542 an SPM toolbox of our algorithm, including the opportunity to adapt
 543 κ , which will be freely available to the scientific community.

544 In summary, we have developed a promising tool for automated
 545 detection of T2-hyperintense lesions in MS based on a modern 3 T
 546 MRI protocol including a 3D GRE T1-weighted and a FLAIR sequence.

547 Disclosure statement

548 The authors declare that there are neither actual nor potential
 549 conflicts of interest.

550 Acknowledgments

551 C.G. is supported by the German BMBF grant 01EV0709. M.A. was
 552 supported by Merck Serono. This work was in part supported by a
 553 grant from the German Ministry for Education and Research (BMBF,
 554 "German Competence Network Multiple Sclerosis" (KKNMS),
 555 Control-MS, 01GI0917).

Appendix A1. Pseudo-code description of the lesion growth algorithm

556
 557

$L = L_{init}$

DO WHILE stopping criterion not satisfied

FOR all voxels i with $\pi_i^{Les} = 0$ that have at least one voxel in
 their neighborhood N_i with $\pi_j^{Les} > 0, j \in N_i$

$$\pi_i^{Les} = \min \left(1, \frac{\rho_{Les} \left(\gamma_i | \hat{\alpha}^{(t-1)}, \hat{\beta}^{(t-1)} \right) \cdot b_i \cdot \exp \left(- \sum_{j \in N_i} (1 - \pi_j^{Les}) \right)}{\rho_{Other} \left(\gamma_i | \hat{\theta}^{(t-1)} \right) \cdot \exp \left(- \sum_{j \in N_i} \pi_j^{Les} \right)} \right)$$

END FOR

UPDATE $\hat{\theta}$, $\hat{\alpha}$ and $\hat{\beta}$

UPDATE stopping criterion

END DO

with

558

B : lesion belief map with values $b_i, i = 1, \dots, n$ (Lesion belief
 maps and initialization section)

559
 560

γ_i : normalized FLAIR intensity of voxel i (Lesion belief maps
 and initialization section)

561
 562

563 p_{Les} : gamma probability density function for the lesion class
 564 with shape and scale parameters alpha and beta, respec-
 565 tively (**Lesion growing section**)
 566 p_{Other} : mixture of three Gaussians for the other tissue classes
 567 (CSF, GM and WM) with parameter vector $\theta = \{\mu_{CSF}, \mu_{GM},$
 568 $\mu_{WM}, \sigma_{CSF}^2, \sigma_{GM}^2, \sigma_{WM}^2\}$ (**Lesion growing section**)
 569 L_{init} : initialized lesion map (**Lesion belief maps and initialization**
 570 **section**)
 571 L : lesion probability map with values $\pi_i^{Les}, i = 1, \dots, n$
 572 N_i : first order neighborhood of voxel i
 573 Stopping criterion: maximal number of iterations or greatest new le-
 574 sion probability <0.01 .
 575

576 Appendix A2. Performance parameters

577 The algorithm performs well on a computer with a 3.2 GHz pro-
 578 cessor and 8 GB RAM. Preprocessing by SPM8 and VBM8 takes
 579 about 10 min, the lesion growth algorithm another 2–3 min depend-
 580 ing on the number of iterations. In our analysis, the median number of
 581 iterations was 16, the maximum 50. We assume that performance is
 582 similar on computers with less memory capacity and processing
 583 power. However, we recommend the use of at least 2 GB RAM.

584 References

585 Ait-Ali, L.S., Prima, S., Hellier, P., Carsin, B., Edan, G., Barillot, C., 2005. STREM: a robust
 586 multidimensional parametric method to segment MS lesions in MRI. In: Duncan,
 587 J.S., Gerig, G. (Eds.), *Medical Image Computing and Computer-Assisted Intervention*
 588 *— Miccai 2005*, pp. 409–416. Pt 1.
 589 Akselrod-Ballin, A., Galun, M., Gomori, J.M., Filippi, M., Valsasina, P., Basri, R., Brandt, A.,
 590 2009. Automatic segmentation and classification of multiple sclerosis in multi-
 591 channel MRI. *IEEE Trans Biomed Eng* 56, 2461–2469.
 592 Anbeek, P., Vincken, K.L., van Osch, M.J., Bisschops, R.H., van der Grond, J., 2004. Probabilis-
 593 tic segmentation of white matter lesions in MR imaging. *Neuroimage* 21, 1037–1044.
 594 Ashburner, J., Friston, K.J., 2000. Voxel-based morphometry—the methods. *Neuroimage*
 595 11, 805–821.
 596 Ashburner, J., Friston, K.J., 2005. Unified segmentation. *Neuroimage* 26, 839–851.
 597 Bagnato, F., Jeffries, N., Richert, N.D., Stone, R.D., Ohayon, J.M., McFarland, H.F., Frank,
 598 J.A., 2003. Evolution of T1 black holes in patients with multiple sclerosis imaged
 599 monthly for 4 years. *Brain* 126, 1782–1789.
 600 Bakshi, R., Ariyaratana, S., Benedict, R.H., Jacobs, L., 2001. Fluid-attenuated inversion re-
 601 covery magnetic resonance imaging detects cortical and juxtacortical multiple
 602 sclerosis lesions. *Arch. Neurol.* 58, 742–748.
 603 Bartko, J.J., 1991. Measurement and reliability: statistical thinking considerations. *Schiz-*
 604 *ophr. Bull.* 17, 483–489.
 605 Bendfeldt, K., Blumhagen, J.O., Egger, H., Loetscher, P., Denier, N., Kuster, P., Traud, S.,
 606 Mueller-Lenke, N., Naegelin, Y., Gass, A., Hirsch, J., Kappos, L., Nichols, T.E., Radue,
 607 E.W., Borgwardt, S.J., 2010. Spatiotemporal distribution pattern of white matter le-
 608 sion volumes and their association with regional grey matter volume reductions in
 609 relapsing–remitting multiple sclerosis. *Hum. Brain Mapp.* 31, 1542–1555.
 610 Chard, D.T., Griffin, C.M., Parker, G.J., Kapoor, R., Thompson, A.J., Miller, D.H., 2002. Brain at-
 611 rophy in clinically early relapsing–remitting multiple sclerosis. *Brain* 125, 327–337.
 612 Compston, A., Coles, A., 2008. Multiple sclerosis. *Lancet* 372, 1502–1517.
 613 Confavreux, C., Vukusic, S., 2008. The clinical epidemiology of multiple sclerosis. *Neu-*
 614 *roimaging Clin. N. Am.* 18, 589–622 ix–x.
 615 Dice, L.R., 1945. Measures of the amount of ecologic association between species. *Ecol-*
 616 *ogy* 26, 297–302.
 617 Ebers, G.C., 1998. Randomised double-blind placebo-controlled study of interferon
 618 beta-1a in relapsing/remitting multiple sclerosis. PRISMS (Prevention of Relapses
 619 and Disability by Interferon beta-1a Subcutaneously in Multiple Sclerosis) Study
 620 Group. *Lancet* 352, 1498–1504.
 621 Ferrari, R.J., Wei, X., Zhang, Y., Scott, J.N., Mitchell, J.R., 2003. Segmentation of multiple
 622 sclerosis lesions using support vector machines. *Proceedings of SPIE* 5032, 16–26.
 623 Filippi, M., Yousry, T., Baratti, C., Horsfield, M.A., Mammì, S., Becker, C., Voltz, R., Spuler,
 624 S., Campi, A., Reiser, M.F., Comi, G., 1996. Quantitative assessment of MRI lesion
 625 load in multiple sclerosis, a comparison of conventional spin-echo with fast
 626 fluid-attenuated inversion recovery. *Brain* 119 (Pt 4), 1349–1355.
 627 Fisher, E., Lee, J.C., Nakamura, K., Rudick, R.A., 2008. Gray matter atrophy in multiple
 628 sclerosis: a longitudinal study. *Ann. Neurol.* 64, 255–265.
 629 Fisniku, L.K., Brex, P.A., Altmann, D.R., Miszkiel, K.A., Benton, C.E., Lanyon, R., Thompson,
 630 A.J., Miller, D.H., 2008. Disability and T2 MRI lesions: a 20-year follow-up of patients
 631 with relapse onset of multiple sclerosis. *Brain* 131, 808–817.
 632 Freifeld, O., Greenspan, H., Goldberger, J., 2009. Multiple sclerosis lesion detection
 633 using constrained GMM and curve evolution. *Int J Biomed Imaging* 2009, 715124.

Garcia-Lorenzo, D., Lecoeur, J., Arnold, D.L., Collins, D.L., Barillot, C., 2009. Multiple scler-
 634 osis lesion segmentation using an automatic multimodal graph cuts. *Med Image*
 635 *Comput Comput Assist Interv* 12, 584–591.
 636 Geremia, E., Menze, B., Clatz, O., Konukoglu, E., Criminisi, A., Ayache, N., 2010. Spatial
 637 decision forests for MS lesion segmentation in multi-channel MR images. *Med*
 638 *Image Comput Comput Assist Interv* 13, 111–118.
 639 Herskovits, E.H., Bryan, R.N., Yang, F., 2008. Automated Bayesian segmentation of mi-
 640 crovascular white-matter lesions in the ACCORD-MIND study. *Adv. Med. Sci.* 53,
 641 182–190.
 642 Jacobs, L.D., Beck, R.W., Simon, J.H., Kinkel, R.P., Brownscheidle, C.M., Murray, T.J., Simonian,
 643 N.A., Slasor, P.J., Sandrock, A.W., 2000. Intramuscular interferon beta-1a therapy
 644 initiated during a first demyelinating event in multiple sclerosis, CHAMPS Study
 645 Group. *N. Engl. J. Med.* 343, 898–904.
 646 Kappos, L., 1998. Placebo-controlled multicentre randomised trial of interferon beta-1b
 647 in treatment of secondary progressive multiple sclerosis. European Study Group on
 648 interferon beta-1b in secondary progressive MS. *Lancet* 352, 1491–1497.
 649 Khayati, R., Vafadust, M., Towhidkhal, F., Nabavi, M., 2008. Fully automatic segmenta-
 650 tion of multiple sclerosis lesions in brain MR FLAIR images using adaptive mixtures
 651 method and Markov random field model. *Comput. Biol. Med.* 38, 379–390.
 652 Landis, J.R., Koch, G.G., 1977. The measurement of observer agreement for categorical
 653 data. *Biometrics* 33, 159–174.
 654 Li, D.K., Held, U., Petkau, J., Daumer, M., Barkhof, F., Fazekas, F., Frank, J.A., Kappos, L.,
 655 Miller, D.H., Simon, J.H., Wolinsky, J.S., Filippi, M., 2006. MRI T2 lesion burden in
 656 multiple sclerosis: a plateauing relationship with clinical disability. *Neurology* 66,
 657 1384–1389.
 658 Li, L., Wei, X., Li, X., Rizvi, S., Liang, Z., 2005. Mixture segmentation of multispectral MR
 659 brain images for multiple sclerosis. *Journal of Systemics, Cybernetics and Informat-*
 660 *ics* 3, 65–68.
 661 Lüders, E., Gaser, C., Narr, K.L., Toga, A.W., 2009. Why sex matters: brain size indepen-
 662 dent differences in gray matter distributions between men and women. *J. Neurosci.*
 663 29, 14265–14270.
 664 Neema, M., Guss, Z.D., Stankiewicz, J.M., Arora, A., Healy, B.C., Bakshi, R., 2009. Normal
 665 findings on brain fluid-attenuated inversion recovery MR images at 3 T. *AJNR Am.*
 666 *J. Neuroradiol.* 30, 911–916.
 667 Noseworthy, J.H., Lucchinetti, C., Rodriguez, M., Weinshenker, B.G., 2000. Multiple scler-
 668 osis. *N. Engl. J. Med.* 343, 938–952.
 669 Polman, C.H., Reingold, S.C., Banwell, B., Clanet, M., Cohen, J.A., Filippi, M., Fujihara, K.,
 670 Havrdova, E., Hutchinson, M., Kappos, L., Lublin, F.D., Montalban, X., O'Connor, P.,
 671 Sandberg-Wollheim, M., Thompson, A.J., Waubant, E., Weinshenker, B., Wolinsky,
 672 J.S., 2011. Diagnostic criteria for multiple sclerosis: 2010 revisions to the McDonald
 673 criteria. *Ann. Neurol.* 69, 292–302.
 674 Rajapakse, J.C., Giedd, J.N., Rapoport, J.L., 1997. Statistical approach to segmentation of
 675 single-channel cerebral MR images. *IEEE Trans. Med. Imaging* 16, 176–186.
 676 Sahraian, M.A., Radue, E.W., Haller, S., Kappos, L., 2009. Black holes in multiple scler-
 677 osis: definition, evolution, and clinical correlations. *Acta Neurol. Scand.*
 678 117, 105–112.
 679 Stevenson, V.L., Gawne-Cain, M.L., Barker, G.J., Thompson, A.J., Miller, D.H., 1997. Imag-
 680 ing of the spinal cord and brain in multiple sclerosis: a comparative study between
 681 fast FLAIR and fast spin echo. *J. Neurol.* 244, 119–124.
 682 Tohka, J., Zijdenbos, A., Evans, A., 2004. Fast and robust parameter estimation for statisti-
 683 cal partial volume models in brain MRI. *Neuroimage* 23, 84–97.
 684 Uebersax, J.S., 1987. Diversity of decision-making models and the measurement of
 685 interrater agreement. *Psychol. Bull.* 101, 140–146.
 686 Van Leemput, K., Maes, F., Vandermeulen, D., Colchester, A., Suetens, P., 2001. Automat-
 687 ed segmentation of multiple sclerosis lesions by model outlier detection. *IEEE*
 688 *Trans. Med. Imaging* 20, 677–688.
 689 Wattjes, M.P., Barkhof, F., 2009. High field MRI in the diagnosis of multiple sclerosis:
 690 high field-high yield? *Neuroradiology* 51, 279–292.
 691 Wattjes, M.P., Lutterbey, G.G., Harzheim, M., Gieseke, J., Traber, F., Klotz, L., Klockgether,
 692 T., Schild, H.H., 2006a. Higher sensitivity in the detection of inflammatory brain le-
 693 sions in patients with clinically isolated syndromes suggestive of multiple sclerosis
 694 using high field MRI: an intraindividual comparison of 1.5 T with 3.0 T. *Eur. Radiol.*
 695 16, 2067–2073.
 696 Wattjes, M.P., Lutterbey, G.G., Harzheim, M., Gieseke, J., Traber, F., Klotz, L., Klockgether,
 697 T., Schild, H.H., 2006b. Imaging of inflammatory lesions at 3.0 Tesla in patients with
 698 clinically isolated syndromes suggestive of multiple sclerosis: a comparison of
 699 fluid-attenuated inversion recovery with T2 turbo spin-echo. *Eur. Radiol.* 16,
 700 1494–1500.
 701 Weiner, H.L., 2009. The challenge of multiple sclerosis: how do we cure a chronic het-
 702 erogeneous disease? *Ann. Neurol.* 65, 239–248.
 703 Wels, M., Huber, M., Hornegger, J., 2008. Fully automated segmentation of multiple
 704 sclerosis lesions in multispectral MRI. *Pattern Recognition and Image Analysis* 18,
 705 347–350.
 706 Woo, J.H., Henry, L.P., Krejza, J., Melhem, E.R., 2006. Detection of simulated multiple
 707 sclerosis lesions on T2-weighted and FLAIR images of the brain: observer perfor-
 708 mance. *Radiology* 241, 206–212.
 709 Wu, Y., Warfield, S.K., Tan, I.L., Wells, W.M., Meier, D.S., van Schijndel, R.A., Barkhof, F.,
 710 Guttmann, C.R., 2006. Automated segmentation of multiple sclerosis lesion sub-
 711 types with multichannel MRI. *Neuroimage* 32, 1205–1215.
 712 Zhang, Y., Brady, M., Smith, S., 2001. Segmentation of brain MR images through a hid-
 713 den Markov random field model and the expectation–maximization algorithm. *IEEE*
 714 *Trans. Med. Imaging* 20, 45–57.
 715 Zijdenbos, A.P., Dawant, B.M., Margolin, R.A., Palmer, A.C., 1994. Morphometric analysis
 716 of white-matter lesions in MR-images — method and validation. *IEEE Trans. Med.*
 717 *Imaging* 13, 716–724.